A first principles study of the effect of (111)-strain on octahedral rotations and structural phases of LaAlO$_3$

Magnus Moreau,[1] Astrid Marthinsen,[2] Sverre M. Selbach,[2] and Thomas Tybell[1,]*

1) Department of Electronics and Telecommunications, NTNU Norwegian University of Science and Technology, 7491 Trondheim, Norway
2) Department of Materials Science and Engineering, NTNU Norwegian University of Science and Technology, 7491 Trondheim, Norway
*E-mail: thomas.tybell@iet.ntnu.no

Abstract

The structural and electronic response of LaAlO$_3$ to biaxial strain in the (111) plane is studied by density functional theory (DFT) and compared to strain in the (001) plane and isostatic strain. For (111)-strain, in-plane rotations are stabilized by compressive strain and out-of-plane rotations by tensile strain. This is an opposite splitting of the modes compared to (001)-strain. Furthermore, for compressive (111)-strain in-plane rotations are degenerate with respect to rotation axis, giving rise to Goldstone-like modes. We rationalize these changes in octahedral rotations by analyzing the V_A/V_B polyhedral volume ratios. Finally, we investigate how strain affects the calculated band gap, and find a 28 % difference between the strain planes under 4 % tension. This effect is attributed to different A-site dodecahedral crystal field splitting for (001)- and (111)-strain.

I. INTRODUCTION

A central trait of the perovskite oxides is their strong structure – property coupling. From a thin film point-of-view this opens the possibility to tune and modify the properties by epitaxial strain. Examples include induced room temperature ferroelectricity in $SrTiO_3$, which is non-polar in bulk,[1] induced metal insulator transitions in manganites,[2] enhanced Curie temperature and polarization in $BaTiO_3$,[3] increased superconducting critical temperature in $La_{2-x}Sr_xCuO_4$,[4] as well as induced multiferroicity in $SrMnO_3$.[5] This makes strain a valuable tool not only for applications, but also for understanding the physics of perovskite oxides.

Particularly interesting is the strain response of the corner-sharing BO_6 octahedra, which is essential to the physical properties of perovskite materials. In general, strain in perovskites can be accommodated by either changes in B-O bond lengths, rotations of the oxygen octahedra or by the formation of dislocations or point defects.[6] In bulk materials octahedral rotations reduce the size of the A-site dodecahedron, thereby mitigating the size mismatch between A and B cations when the Goldschmidt tolerance factor is below unity.[7] Generally it has been shown that compressive strain in the (001)-plane increases the rotations around the out-of-plane axis, and reduces rotations around in-plane directions, while for tensile strain in the (001)-plane the rotations around in-plane directions increases.[7-10] It has further been shown that these effects can be tuned by changing the out-of-plane lattice parameter through strain doping by light noble elements such as He.[11]

Recent advances in thin film technology have opened up for high quality epitaxial growth along other crystallographic facets, such as [111].[12] The (111)-interface is interesting because of its buckled honeycomb lattice can result in exotic topological states,[13] strong magnetic reconstructions due to a reduced interlayer distance,[14] and strong octahedral coupling as compared to the (001)-interface.[15] The pseudocubic rotation axes of the oxygen octahedra are neither parallel nor perpendicular to the strain plane for (111)-oriented strain, which is the case for (001)-oriented strain (Fig. 1 a-b), expected to affect the strain relaxation mechanism. Strain engineering based on the (111)-plane is however less studied compared to strain applied in the (001)-plane. The studies that do exist have e.g. shown experimentally that (111)-strain preserves the bulk rhombohedral symmetry of $BiFeO_3$, where (111)-strain gave a single domain polar phase, while (001)- and (110)-strain resulted in monoclinic phases.[16] Density functional theory (DFT) studies of $BaTiO_3$ and $PbTiO_3$ have shown that the effect on the electric polarization depends strongly on whether the strain is in the (001)- or the (111)-plane.[17] (111)-strain in $SrTiO_3$ was further found to be viable route to tailor the electronic band gap for optoelectronic devices.[18] While, recently it was shown experimentally that strained $LaNiO_3(111)$ can result in a polar metal.[19] Still, as the octahedral rotations are essential for the properties of many perovskites, there is,

to the best of our knowledge, no systematic study of how octahedral rotations behave when strained in the (111)-plane as compared to the (001)-plane.

In this work DFT is used to study how the octahedral rotations are affected by biaxial strain in the (111)-plane and compared to (001)-strain. To this extent $LaAlO_3$ (LAO) is chosen as model system as bulk LAO only exhibit rotational distortions with no Jahn-Teller or ferroelectric instabilities. The choice is further motivated by the findings of a quasi 2-dimensional electron gas at the (001)-interface between LAO and $SrTiO_3$,[20] which has later been extended to also include the (111)-interface.[21] The octahedral response of LAO to (001)-strain is well established.[9,10] For strain in the (001)-plane, even small values of strain changes symmetry away from bulk $R\bar{3}c$ which has octahedral rotations around the [111] axis. Compressive strain results in $I4/mcm$ symmetry with rotations around the [001] out-of-plane axis, and tensile strain in $Imma$ with rotations around the [110] in-plane axis.[9,10] We show that strain along the (111) facet results in different crystallographic phases with different octahedral rotation patterns as compared to (001)-strain, where the in-plane rotations are stabilized by compressive strain, while out-of-plane rotations are stabilized by tensile strain. Furthermore, any combination of the two stabilized orthogonal in-plane rotations for (111)-strain are degenerate, giving rise to Goldstone-like modes. The choice of strain plane also affects the orbital splitting, and in LAO this manifests as significant changes to the band gap. The paper is structured as follows: In section II the calculation details are given. Section III discusses the different crystalline phases that are stable for different values of strain, followed by section IV where we discuss how the octahedral rotations depend on strain and compare it to the calculated polyhedral volume ratio. Finally, in section V the effect of strain plane on crystal field splitting of the orbital energies and the electronic band gap is discussed.

II. COMPUTATIONAL DETAILS

The calculations were performed with the projected augmented wave (PAW) method[22,23] as implemented in the Vienna Ab-initio Simulation package (VASP).[23,24] All relaxations were done with the Perdew-Burke-Ernzerhof generalized gradient approximation for solids (PBE-sol) functional, which has been shown to give better results than the standard PBE for structural relaxations.[25] The PAW-potentials with electron configurations $4s^2 4p^6 5d^1 6s^2$, $3s^2 3p^1$ and $2s^2 2p^4$ were used for the La, Al and O respectively, while the plane wave cut off was set to 550 and 800 eV for (001) and (111)-strain respectively. The GGA+U (Dudarev et al.[26]) with U=10 eV was applied to the La f-states, in order to move them away from the bottom of the conduction band,[10,27] this assumption was later confirmed by the hybrid functional calculations, which were done with the HSE-sol functional.[28]

To simulate the effect of epitaxial strain, the in-plane lattice parameters were locked, while the out-of-plane lattice parameter was allowed to relax. We define (001)-strain and (111)-strain as strain in the (001)-plane and (111)-plane, respectively. Strain is calculated as $\epsilon_\parallel = (a - a_0)/a_0$ where a is the enforced in plane lattice parameter, and a_0 is equilibrium PBE-sol lattice parameter along the [100] and [010], or [1$\bar{1}$0] and [10$\bar{1}$] pseudocubic directions depending on strain plane, see Fig. 1 c) and d). Quadratic strain was assumed for all calculations. Constant volume calculations were used to calculate the effects of hydrostatic pressure. The internal coordinates of the ions and the out-of-plane lattice parameter were relaxed until the forces on the ions were below 10 and 1 meV/f.u for (001)- and (111)-strain respectively. We allowed less strict convergence for (001)-strain as our calculations were in excellent agreement with the results from Hatt and Spaldin.[9] The calculations for strain in (001)-plane were done with a 40 atom $2 \times 2 \times 2$ supercell (Fig. 1c) to allow for all types of octahedral rotations, in this structure lattice vectors a, b and c are along the [100], [010] and [001] pseudocubic directions respectively. While for the calculations for strain in the (111)-plane and for the calculations with constant volume were done with a 30 atom $\sqrt{2} \times \sqrt{2} \times 2\sqrt{3}$ supercell (Fig. 1d), where a, b and c lattice vectors are along the [1$\bar{1}$0], [10$\bar{1}$] and [111] pseudocubic directions respectively. For the 40 atom $2 \times 2 \times 2$ supercell a $4 \times 4 \times 4$ k-point Γ-centered mesh was used to sample the Brillouin zone, while for the 30 atom $\sqrt{2} \times \sqrt{2} \times 2\sqrt{3}$ supercell, a $6 \times 6 \times 3$ Γ-centered k-point mesh was used. Phonon calculations were performed utilizing the frozen phonon approach[29] and analyzed with the phonopy software.[30] The phonon calculations were performed with $2 \times 2 \times 2$ supercells of the ideal 5 atom perovskite structure; $Pm\bar{3}m$ symmetry for the unstrained cells, and $P4/mmm$ and $R\bar{3}m$ for (001)- and (111)-strain, respectively. These cells were relaxed until the energy difference between subsequent ionic steps were lower than 10^{-8} eV. The determination of space groups where done with the FINDSYM software with a tolerance of 0.005 Å.[31]

Rotations angles α, β and γ about the pseudocubic axes x, y and z respectively, are defined as shown in Fig. 1 a and b). For (001)-strain, the x and y directions are in the strain plane, while z is out-of-plane, while for (111)-strain none of the directions are perpendicular or parallel to the strain plane. All crystallographic directions are given in the pseudocubic setting unless otherwise stated.

III. STRUCTURAL PHASES

LAO has $R\bar{3}c$ symmetry which deviates from the aristotype cubic $Pm\bar{3}m$ perovskite with anti-phase rotations around one of the pseudocubic ⟨111⟩-axes ([111], [11$\bar{1}$], [1$\bar{1}$1], or [$\bar{1}$11]), which can be described in the Glazer tilt system as $a^-a^-a^-$.[32] The equilibrium structure based on our calculations has lattice parameters of a = 5.384 Å (pseudocubic 3.807 Å), c = 13.146 Å (pseudocubic 3.795 Å) in the hexagonal setting, and has rotations of the oxygen octahedra around the [111] axis of 4.75°, all in good

agreement with litterature.[33] Hydrostatic pressure results in a decrease of the rotation angle, and for compressive isostatic strain of more than 2 %, the cubic $Pm\bar{3}m$ phase is lower in energy than $R\bar{3}c$. This is also in good agreement with experiments on bulk LAO where the rotation angles decrease with increasing hydrostatic pressure until a phase transition to cubic $Pm\bar{3}m$ occurs at 14 GPa.[34] This hydrostatic pressure corresponds to a compression of all lattice parameters of about 2 %, in good agreement with our calculated isostatic strain at the phase transition.

To investigate the effect of strain on lattice distortions the phonon frequencies were calculated for cubic LAO under both (001)- and (111)-strain, focusing on the unstable modes with imaginary frequencies. For 0 % strain, three degenerate lattice instabilities were found at the *R*-point of the 5-atom $Pm\bar{3}m$ cell. These instabilities correspond to anti-phase rotations, as expected since LAO bulk displays an $a^-a^-a^-$ tilt pattern. As illustrated in Fig. 2, when the structure is strained either in the (001)- or the (111)-pane, these rotational modes are split into orthogonal in-plane and out-of-plane modes. Figure 3 shows how the strain affects the phonon frequencies. As expected, compressive (001)-strain favors rotations around the [001] out-of-plane axis, while tensile strain favors rotations around the in-plane [100] and [010] axes, as seen in Fig. 3 a). Further, as shown in in Fig. 3b), (111)-strain splits the three degenerate modes at 0 % strain into out-of-plane [111]-rotations and in-plane [1$\bar{1}$0] and [11$\bar{2}$] rotations. However, we note that the splitting of in-plane and out-of-plane rotations is opposite with respect to (001)-strain. Under compressive (111)-strain in-plane rotations are favored, while for tensile (111)-strain out-of-plane rotations are favored.

To identify which possible space groups are stable under applied strain, the effect of freezing in different rotational modes is investigated. For (001)-strain, this results in a tetragonal $I4/mcm$ symmetry for the out-of-plane mode with rotations around [001], while the in-plane [100] and [010] rotations stabilized by tensile (001)-strain both result in an orthorhombic $Fmmm$ symmetry, while a superposition with equal amount of [100] and [010] rotations gives an *Imma* symmetry. For the out-of-plane [111]-rotations stabilized by tensile (111)-strain we find a rhombohedral $R\bar{3}c$ symmetry, similar to bulk LAO. While the rotations around the in-plane [1$\bar{1}$0] and [11$\bar{2}$] axes yield monoclinic $C2/m$ and $C2/c$ symmetry, respectively, an arbitrary combination of rotations about the [1$\bar{1}$0] and [11$\bar{2}$] axes results in $P\bar{1}$ symmetry.

From this we calculate the phase diagram as a function of (001)- and (111)-strain. The results are shown in Fig. 4. For (001)-strain, the results reported by Hatt and Spaldin are reproduced.[9] For compressive (001)-strain the tetragonal $I4/mcm$, with rotations around the [001] axis, Glazer tilt pattern $a^0a^0c^-$, has the lowest energy, while for tensile strain the tetragonal *Imma* structure, with tilt pattern $a^-a^-c^0$, has the lowest energy. For small levels of (001)-strain (± 0.25 %) LAO accommodates a monoclinic

$C2/c$ structure. This $C2/c$ structure is similar to the $R\bar{3}c$ space group but has tilt pattern $a^-a^-c^-$ instead of $a^-a^-a^-$, as the out-of-plane lattice parameter is no longer equal to the in-plane lattice parameter and any perturbation from the unstrained system has to change the symmetry. However, as the deviation from the $R\bar{3}c$ space group is small within the limited strain window where this $C2/c$ structure is stable, we will label it as $R\bar{3}c$ for the rest of this paper. For (111)-strain, as shown in Fig. 4 b), tensile strain preserves the bulk $R\bar{3}c$ symmetry. In this case the rotation axes of the octahedra are now always perpendicular to the strain plane, i.e. the four ⟨111⟩-axes are no longer degenerate. Also in accordance with the phonon calculations, for compressive (111)-strain the three different monoclinic phases ($C2/m$, $C2/c$ and $P\bar{1}$) are degenerate. The energy differences between these three phases are calculated to be less than 0.1 meV/formula unit (f.u.). Also, these three monoclinic phases are lower in energy than the bulk $R\bar{3}c$ phase for all compressive strain values considered. The structural parameters from the different phases for representative values of strain are shown in Table I.

Another difference between (001)- and (111)-strained LAO is the difference in out-of-plane lattice parameter response as shown in Fig. 5. Epitaxial thin films generally compensate for tensile (compressive) strain by reducing (increasing) the out-of-plane lattice parameter. We quantify this by estimating the Poissons ratio, and LAO strained in the (001)-plane have a significantly larger Poissons ratio, 0.265-0.305, as compared to LAO strained in the (111)-plane, 0.178-0.195. This value for (001)-strain is closer to the experimental bulk value of 0.26.[35] Hence, strain in the (001)-plane is more prone to preserve the volume.

As shown in Fig. 3, the two in-plane modes have degenerate phonon frequencies, indicating that the 2nd order terms in a harmonic approximation are equal.[36] However, the 4th order terms does not need to be equal, which in turn could make certain in-plane rotation axes favored. Hence, to investigate if there are favored in-plane directions for the rotations, the two in-plane modes are simultaneously frozen to identify possible combinations giving an energy lowering. Figure 6 depicts the energy landscape from such calculations of the degenerate modes for 1 % tensile (001)-strain and 1 % compressive (111)-strain. For tensile (001)-strain it is found that the global minimum is for an equal amount of [100]- and [010]-rotations, resulting in a tetragonal $Imma$ structure with rotations around [110] (Fig. 6c). In contrast, no single global minimum for combinations of [1$\bar{1}$0] and [11$\bar{2}$] rotations is found under compressive (111)-strain. Instead, a circle of continuous minima is obtained, resulting in a Mexican hat shaped energy surface. Any arbitrary point along the circle corresponds to the space group $P\bar{1}$, which is a subgroup of both $C2/c$ and $C2/m$. We note such a circular energy landscape as under (111)-compression is compatible with Goldstone-like modes.[37] While such modes are common in *isotropic* materials, few experimentally observations are available for *anisotropic* crystals, with one

exception being superconducting $Cd_2Re_2O_7$.[38] Goldstone-like modes have been proposed to occur in carefully engineered ferroelectric Ruddlesden-Popper phases from DFT calculations.[39] Further we note that under quadratic (111)-strain there is only 30° between symmetry equivalent axes of the orthogonal rotations ($\langle 1\bar{1}0 \rangle$ and $\langle 11\bar{2} \rangle$), while for (001)-strain these axes ($\langle 100 \rangle$ and $\langle 010 \rangle$) are separated by 90°. Hence, it is possible that the underlying energy landscape is not a perfect circle, but instead a regular dodecagon where the energy differences between possible local minima and maxima are less than 0.1 meV/f.u., lower than the resolution of the DFT-calculations.

From a thin film perspective, by relying on compressive (111)-strain, there is no apparent driving force for domain formation, e.g. it should be possible to synthesize compressively (111)-strained structurally monodomain LAO thin films. However, the choice of substrate could lift this degeneracy, either through imprinting the rotation pattern of the substrate, or through non-quadratic strain from e.g. an orthorhombic substrate.

IV. OCTAHEDRAL ROTATIONS AND POLYHEDRAL VOLUME RATIO

We now turn to how the strain is mitigated through octahedral rotations in the different phases by comparing the rotations projected on the pseudocubic axes. Figure 7 shows how the strain affects the rotations for the different symmetries as a function of (001)- and (111)-strain. For the (001)-strain, in Fig. 7 a), the tilt pattern switches from the bulk $a^-a^-a^-$ tilt pattern to $a^0a^0c^-$ for compressive strain, and to $a^-a^-c^0$ outside the small window (± 0.25 %) where the $a^-a^-a^-$ tilt is stable. We further confirm that the rotation amplitudes of the respective phase behaves approximately linear for increasing absolute value of strain, as reported by Hatt and Spaldin.[9] However, for (111)-strain, in Fig. 7 b-d) a different trend is observed. For tensile strain in the (111)-plane, which preserves the $R\bar{3}c$ symmetry, the rotations around the pseudocubic axes are almost constant at 2.65° each, corresponding closely to the bulk rotation value around the [111] axis of 4.75°. The small changes in the rotation angles can be attributed to the fact that none of the pseudocubic directions are perpendicular or parallel to the strain plane, effectively locking the rotations with (111)-strain. For compressive strain in the (111)-plane we find that as the rhombohedral symmetry is lifted, the crystal has larger possibilities to accommodate the strain through octahedral rotations. As seen in Fig. 7 b) and c), the $C2/m$, $C2/c$ structures have rotation patterns $a^-a^-c^0$ and $a^-a^-c^-$, corresponding to rotations around the in-plane $[1\bar{1}0]$ and $[11\bar{2}]$ axes, respectively (note that for the rotations around $[11\bar{2}]$ in Fig. 7 c) the α and β rotations are $\sim$ half the γ rotations) . The evolution of the pseudocubic rotation angles for of one of the arbitrary combinations of in-plane $[1\bar{1}0]$ and $[11\bar{2}]$ rotation with $P\bar{1}$ symmetry is depicted in Fig 7 d), where this illustrated specific combination of rotations has an $a^-b^-c^-$ tilt pattern. Even though the rotation patterns are different, their response to strain is similar in the

sense that the largest rotation for all three tilt patterns is about 3° for -0.25 % (111)-strain and decreases to about 2° for -4 % strain.

To better understand the anisotropic effects of strain a comparison to calculations with isostatic strain emulating hydrostatic pressure is performed, the results are shown in Fig. 7e). For the degenerate LAO phases, the rotation amplitude decreases monotonically with increasing compressive strain, Fig. 7 b-d). This is qualitatively similar the response to hydrostatic pressure,[34] and is attributed to the higher compressibility of the Al^{3+} octahedra than the La^{3+} dodecahedra, as is commonly found for III-III perovskites.[40] We note that even though the rotation amplitudes are reduced for (111)-compression, a possible phase without any rotations such as $R\bar{3}m$ or $Pm\bar{3}m$ is never obtained for the range of strain range considered here This is in contrast with the response of hydrostatic pressure, Fig. 7 e), resulting in a $Pm\bar{3}m$ phase for compressive strain larger than 2%.

In order to better quantify how strain distorts the crystal we have calculated the polyhedral volume ratio V_A/V_B, the volume of the A-site dodecahedron divided by the volume of the B-site octahedron. The ratio V_A/V_B is equal to 5.0 for the cubic structure without octahedral tilt, and the deviation from 5.0 is proportional to the degree of structural distortion.[41,42] The polyhedral volume ratio as a function of strain in the (001)- and (111)-planes is shown in Fig. 8, as well as how it changes for isostatic strain. For (001)- and (111)-strain, Fig. 8 a-b), a clear trend is seen that the phase with the most distorted crystal structure, the lowest V_A/V_B, also has the lowest energy. This trend is different from what is observed when the polyhedral volume ratio is studied experimentally as a function of temperature or pressure, for which the different space groups have different ranges of V_A/V_B for where the different distortions are stable, giving rise to steps in the V_A/V_B ratio.[41,43] The reason why (001)-strain favors out-of-plane rotations under compression and in-plane rotations under tension, while it is opposite for (111)-strain, can now be explained as the structure minimizing the V_A/V_B ratio. Considering that while the stacking sequence in the perovskite structure along the [001]-direction is $AO \rightarrow BO_2 \rightarrow AO \rightarrow BO_2 \rightarrow \cdots$, along the [111]-direction it is $AO_3 \rightarrow B \rightarrow AO_3 \rightarrow B \rightarrow \cdots$. Hence, to optimize the coordination of the small A-cation under (111)-strain without increasing the V_A/V_B ratio, the oxygen atoms are pushed up and down by the in-plane octahedral rotations under compressive strain. Under (111)-tensile strain there is a possibility to move in the strain plane, as illustrated by the black arrows in Fig. 2b). This differs from the situation under (001)-strain where the oxygen movements are in the same directions as the compression when the V_A/V_B ratio is minimized. Finally we note that the $R\bar{3}c$ structure has a similar response to (111)-strain and hydrostatic pressure, see Fig. 8 b) and c). I.e. tensile strain in the (111) plane of perovskites gives the same distortions as under negative isostatic pressure, which is not easily accessible by experiments.

It is now possible to rationalize the increased energy cost for straining in the (111)-plane as compared to (001)-strain. The total energy as a function of strain, see Fig. 4, can be fitted to the equation $E = A\epsilon_\parallel^2 + B\epsilon_\parallel + C$, where $\epsilon_\parallel$ is the in-plane strain and A, B and C are the fitting parameters. For (111)-strain we find that $A_{111} \approx 16$ meV/%^{2}-f.u. while for (001) $A_{001} \approx 12$ meV/%^{2}-f.u. is obtained. This can be understood by considering the fact that when strain is applied in the (001) plane, the structure can more easily compensate for changes in strain by rotating the oxygen octahedra as compared to strain in the (111)-plane, as the oxygen movements are in the same directions as the structure is compressed. This effect is also observed when taking into account the larger Poissons ratio for (001)-strain, meaning that (001)-strain has smaller changes in volume for increasing compressive or tensile strain.

V. ORBITAL SPLITTING AND BAND GAP

Having established how (001)- and (111)-strain affects the symmetry and octahedral rotations of LAO we turn to how strain affects the electronic properties. The band gap in LAO is between the occupied O$_{2p}$ states in the valence band and empty La$_{5d}$ states in the conduction band[27] (see supplementary info for the projected density of states of the hybrid functional calculations). It is known that the different strain planes affects the crystal field splitting of d-states. As shown for dodecahedral sites in Fig. 9, the cubic distortion from (001)-strain, splits both the top t_{2g} and the bottom e_g levels, while the trigonal distortion from (111)-strain only splits the top t_{2g} states[44] (for illustration of the dodecahedrally coordinated d states see supplementary information). This change in crystal field splitting does indeed affect the electronic properties. In Fig. 10 the PBE-sol band gap is plotted vs strain in the (001)- and (111)-plane, and compared to the results for isostatic strain. As seen, the band gap for (001)-strain is decreasing for both tensile and compressive strain, while for (111)-strain the band gap is decreasing for compressive strain and increasing for tensile strain, similar to the effect of hydrostatic pressure. Since the trend is opposite for tensile (001)- and (111)-strain, LAO has a significant different band gap for different strain planes, ~ 0.8 eV at 4% tensile strain, corresponding to a change of 28 %. There is also a slight difference in band gap between the degenerate monoclinic phases, where $C2/c$ has the highest band gap followed by $P\bar{1}$ and $C2/m$. However, these differences are below 0.1 eV for 0.25 % compressive strain, and are further reduced for increasing compressive strain, due to all the rotation angles being reduced; thus the structures becoming more and more similar.

The difference between (001)- and (111)-strain, as well as the reason why (111)-strain behaves as if under hydrostatic pressure can be understood by considering the orbital splitting differences between (001)- and (111)-strain. Under strain in the (001)- and (111)-plane the $5d$ states of the 12 coordinated La are split as shown in Fig. 9. As the (111)-strain only splits the top orbitals in the top of the conduction

9

band, the changes observed in the band gap are dominated by changes in interatomic distances, similar to what is seen for hydrostatic pressure. For (001)-strain the effect of change in interatomic distances is also present, but it is superimposed on the stronger effect of splitting of the e_g orbitals; thus the band gap is reduced also for tensile (001)-strain, however less compared to compressive (001)-strain. This is all summarized in schematic density of states (DOS) shown in Fig. 11. A difference in calculated band gap between (001)- and (111)-strain were also reported for $SrTiO_3$. However, for $SrTiO_3$ the effect were attributed to suppression of ferroic distortions[18] instead of different orbital splitting as we show here.

VI. CONCLUSIONS

Epitaxial strain in the (001)- and (111)-plane is non-equivalent. (001)-strain is known to favor tetragonal phases with out-of-plane rotations for compressive strain and in-plane rotations for tensile strain. As we have shown, this trend is opposite for LAO under (111)-strain where compressive strain favors in-plane rotations and tensile strain favors out-of-plane rotations. Further, we have shown that the in-plane rotation directions for (111)-strain are degenerate giving rise to Goldstone-like modes. The fact that strain in the (111)-plane can result in degenerate LAO phases having different octahedral tilt patterns has implications for other rhombohedral materials systems where the functional properties is strongly coupled to the octahedral rotations, such as $(La,Sr)MnO_3$.[45] Due to the different orbital splitting from (001)- and (111)-strain, the band gap of LAO depends on the strain plane, giving a change in PBE-sol band gap of 28 % for 4 % tensile strain depending on the strain plane. This significant difference in band gap needs be taken into account when designing functional [111] oriented superlattices based on effects such as charge transfer. Hence epitaxial (111)-oriented thin films is an exciting avenue for tailoring systems with different octahedral responses, and opens up new ways to tailor band gaps e.g. for optoelectronic devices.

References

[1] J. H. Haeni, P. Irvin, W. Chang, R. Uecker, P. Reiche, Y. L. Li, S. Choudhury, W. Tian, M. E. Hawley, B. Craigo *et al.*, Nature **430**, 758 (2004).

[2] K. H. Ahn, T. Lookman, and A. R. Bishop, Nature **428**, 401 (2004).

[3] K. J. Choi, M. Biegalski, Y. L. Li, A. Sharan, J. Schubert, R. Uecker, P. Reiche, Y. B. Chen, X. Q. Pan, V. Gopalan *et al.*, Science **306**, 1005 (2004).

[4] I. Bozovic, G. Logvenov, I. Belca, B. Narimbetov, and I. Sveklo, Phys. Rev. Lett. **89**, 107001 (2002).

[5] J. H. Lee and K. M. Rabe, Phys. Rev. Lett. **104**, 207204 (2010).

[6] U. Aschauer, R. Pfenninger, S. M. Selbach, T. Grande, and N. A. Spaldin, Phys. Rev. B **88**, 054111, 054111 (2013).

[7] J. M. Rondinelli and N. A. Spaldin, Adv. Mat. **23**, 3363 (2011).

[8] A. T. Zayak, X. Huang, J. B. Neaton, and K. M. Rabe, Phys. Rev. B **74**, 094104 (2006).

[9] A. J. Hatt and N. A. Spaldin, Phys. Rev. B **82**, 195402 (2010).

[10] R. L. Johnson-Wilke, D. Marincel, S. Zhu, M. P. Warusawithana, A. Hatt, J. Sayre, K. T. Delaney, R. Engel-Herbert, C. M. Schlepuetz, J. W. Kim *et al.*, Phys. Rev. B **88**, 174101, 174101 (2013).

[11] A. Herklotz, A. T. Wong, T. Meyer, M. D. Biegalski, H. N. Lee, and T. Z. Ward, Sci. Rep. **6**, 26491 (2016).

[12] I. Hallsteinsen, J. E. Boschker, M. Nord, S. Lee, M. Rzchowski, P. E. Vullum, J. K. Grepstad, R. Holmestad, C. B. Eom, and T. Tybell, J. Appl. Phys. **113**, 183512, 183512 (2013).

[13] D. Doennig, W. E. Pickett, and R. Pentcheva, Phys. Rev. Lett. **111**, 126804 (2013); Y. Weng, X. Huang, Y. Yao, and S. Dong, Phys. Rev. B **92**, 195114 (2015).

[14] M. Gibert, P. Zubko, R. Scherwitzl, J. Íñiguez, and J.-M. Triscone, Nat. Mater. **11**, 195 (2012); C. Piamonteze, M. Gibert, J. Heidler, J. Dreiser, S. Rusponi, H. Brune, J. M. Triscone, F. Nolting, and U. Staub, Phys. Rev. B **92**, 014426 (2015).

[15] I. Hallsteinsen, M. Moreau, A. Grutter, M. Nord, P. E. Vullum, D. A. Gilbert, T. Bolstad, J. K. Grepstad, R. Holmestad, S. M. Selbach *et al.*, Phys. Rev. B **94**, 201115 (2016).

[16] J. F. Li, J. L. Wang, M. Wuttig, R. Ramesh, N. Wang, B. Ruette, A. P. Pyatakov, A. K. Zvezdin, and D. Viehland, Appl. Phys. Lett. **84**, 5261 (2004).

[17] A. Raeliarijaona and H. Fu, J. Appl. Phys. **115**, 054105 (2014); R. Oja, K. Johnston, J. Frantti, and R. M. Nieminen, Phys. Rev. B **78**, 094102 (2008).

[18] R. F. Berger, C. J. Fennie, and J. B. Neaton, Phys. Rev. Lett. **107**, 146804 (2011).

[19] T. H. Kim, D. Puggioni, Y. Yuan, L. Xie, H. Zhou, N. Campbell, P. J. Ryan, Y. Choi, J. W. Kim, J. R. Patzner *et al.*, Nature **533**, 68 (2016).

[20] A. Ohtomo and H. Y. Hwang, Nature **427**, 423 (2004).

[21] G. Herranz, F. Sánchez, N. Dix, M. Scigaj, and J. Fontcuberta, Sci. Rep. **2**, 758 (2012).

[22] P. E. Blochl, Phys. Rev. B **50**, 17953 (1994).

[23] G. Kresse and D. Joubert, Phys. Rev. B **59**, 1758 (1999).

[24] G. Kresse and J. Furthmuller, Phys. Rev. B **54**, 11169 (1996).

[25] J. P. Perdew, A. Ruzsinszky, G. I. Csonka, O. A. Vydrov, G. E. Scuseria, L. A. Constantin, X. L. Zhou, and K. Burke, Phys. Rev. Lett. **100**, 136406, 136406 (2008).

[26] S. L. Dudarev, G. A. Botton, S. Y. Savrasov, C. J. Humphreys, and A. P. Sutton, Phys. Rev. B **57**, 1505 (1998).

[27] S.-G. Lim, S. Kriventsov, T. N. Jackson, J. H. Haeni, D. G. Schlom, A. M. Balbashov, R. Uecker, P. Reiche, J. L. Freeouf, and G. Lucovsky, J. Appl. Phys. **91**, 4500 (2002).

[28] L. Schimka, J. Harl, and G. Kresse, J. Chem. Phys **134**, 024116 (2011).

[29] K. Kunc and R. M. Martin, Phys. Rev. Lett. **48**, 406 (1982).

[30] A. Togo and I. Tanaka, Scripta Materialia **108**, 1 (2015).

[31] H. T. Stokes and D. M. Hatch, J. Appl. Crystallogr. **38**, 237 (2005).

[32] A. Glazer, Acta Crystallogr. Sect. B **28**, 3384 (1972); A. Glazer, Acta Crystallogr. Sect. A **31**, 756 (1975).

[33] K. A. Müller, W. Berlinger, and F. Waldner, Phys. Rev. Lett. **21**, 814 (1968).

[34] P. Bouvier and J. Kreisel, J. Phys.: Condens. Matter **14**, 3981 (2002); M. Guennou, P. Bouvier, G. Garbarino, and J. Kreisel, J. Phys.: Condens. Matter **23**, 395401 (2011).

[35] X. Luo and B. Wang, J. Appl. Phys. **104**, 073518 (2008).

[36] W. Cochran, Phys. Rev. Lett. **3**, 412 (1959).

[37] J. Goldstone, A. Salam, and S. Weinberg, Phys. Rev. **127**, 965 (1962).

[38] C. A. Kendziora, I. A. Sergienko, R. Jin, J. He, V. Keppens, B. C. Sales, and D. Mandrus, Phys. Rev. Lett. **95**, 125503 (2005); J. C. Petersen, M. D. Caswell, J. S. Dodge, I. A. Sergienko, J. He, R. Jin, and D. Mandrus, Nat. Phys. **2**, 605 (2006).

[39] S. M. Nakhmanson and I. Naumov, Phys. Rev. Lett. **104**, 097601 (2010).

[40] R. J. Angel, J. Zhao, and N. L. Ross, Phys. Rev. Lett. **95**, 025503 (2005); J. Zhao, N. L. Ross, and R. J. Angel, J. Phys.: Condens. Matter **16**, 8763 (2004); T. Tohei, A. Kuwabara, T. Yamamoto, F. Oba, and I. Tanaka, Phys. Rev. Lett. **94**, 035502 (2005).

[41] M. Avdeev, E. a. N. Caspi, and S. Yakovlev, Acta Crystallogr. Sect. B **63**, 363 (2007).

[42] N. Thomas, Acta Crystallogr. Sect. B **52**, 16 (1996); N. Thomas, Acta Crystallogr. Sect. B **52**, 954 (1996).

[43] S. M. Selbach, J. R. Tolchard, A. Fossdal, and T. Grande, J. Solid State Chem. **196**, 249 (2012).

[44] D. I. Khomskii, *Transition Metal Compounds* (Cambridge University Press, 2014).

[45] Z. Liao, M. Huijben, Z. Zhong, N. Gauquelin, S. Macke, R. J. Green, S. Van Aert, J. Verbeeck, G. Van Tendeloo, K. Held *et al.*, Nat. Mater. **15**, 425 (2016).

[46] K. Momma and F. Izumi, J. Appl. Crystallogr. **44**, 1272 (2011).

Tables

TABLE I, summary of the calculated structural parameters of different phases at representative values of strain. The rotations are given in the Glazer tilt notation.[32] Note that the labels a, b and c are here the conventional lattice parameters of the given space groups, not the pseudocubic lattice parameters. Further, α, β and γ are here the conventional cell angles, not the rotations of the oxygen octahedral around the different pseudocubic axes.

	Rotations	Strain	a [Å]	b [Å]	c [Å]	α [°]	β [°]	γ [°]	Wyckoff pos.	x	y	z
$R\bar{3}c$	$a^-a^-a^-$	Unstrained	5.385	5.385	13.146	90	90	120	La (6a)	0	0	0.25
									Al (6b)	0	0	0
									O (18e)	0.4760	0	0.25
$I4/mcm$	$a^0a^0c^-$	-1 % (001)	5.325	5.325	7.677	90	90	90	La (4b)	0	0.5	0.25
									Al (4c)	0	0	0
									O (8h)	0.2709	0.7709	0
									O (4a)	0	0	0.25
$Imma$	$a^-a^-c^0$	+1 % (001)	7.544	5.433	5.433	90	90	90	La (4b)	0	0.25	0.74996
									Al (4c)	0.25	0.25	0.25
									O (8f)	0.2333	0	0
									O (4e)	0	0.25	0.2829
$C2/m$	$a^-a^-c^0$	-1 % (111)	9.235	5.332	5.380	90	124.905	90	La (4i)	0.7496	0	0.7494
									Al (2b)	0	0.5	0
									Al (2c)	0	0	0.5
									O (8j)	-0.0138	0.2502	0.7361
									O (4i)	0.2500	0	0.7774
$C2/c$	$a^-a^-c^-$	-1 % (111)	9.235	5.332	7.574	90	144.375	90	La (4e)	0	0.0003	0.25
									Al (4b)	0	0.5	0
									O (8f)	0.7651	0.2349	0.7736
									O (4e)	0	0.5166	0.25
$P\bar{1}$	$a^-b^-c^-$	-1 % (111)	5.332	5.332	5.380	90	119.707	120	La (2i)	-0.0005	0.2496	0.2498
									Al (1f)	0.5	0	0.5
									Al (1e)	0.5	0.5	0
									O (2i)	0.4697	0.2285	0.2284
									O (2i)	-0.0001	0.2549	0.7247
									O (2i)	0.4798	0.7338	0.2460
$R\bar{3}c$	$a^-a^-a^-$	+1 % (111)	5.439	5.439	13.086	90	90	120	La (6a)	0	0	0.25
									Al (6b)	0	0	0
									O (18e)	0.5299	0	0.25
$Pm\bar{3}m$	$a^0a^0a^0$	-2 % isostatic	3.7272	3.7272	3.7272	90	90	90	La (1b)	0.5	0.5	0.5
									Al (1a)	0	0	0
									O (3d)	0.5	0	0

Figures

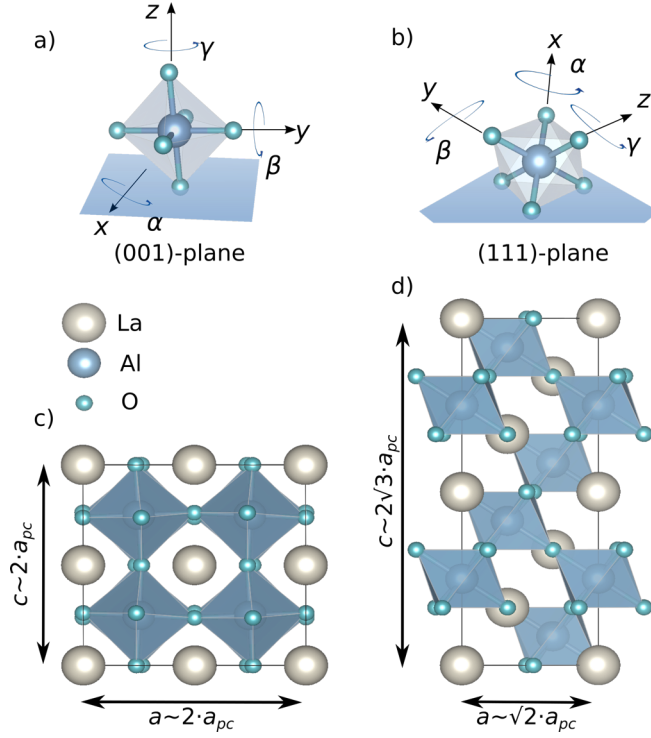FIG 1, a) and b) show the definition of the rotation axes for (001)- and (111)-strain respectively. For (001)-strain the x- and y-axes are parallel to the strain plane, while the z-axis is perpendicular to the strain plane. For (111)-strain, neither the x-, y-, or z-axes are parallel or perpendicular to the strain plane. Note that under the assumption of quadratic strain, the assignment of x, y and z for (111) - train is arbitrary. c) The 40-atom cell used for (001)-strain calculations. d) The 30-atom unit cell used for (111)-strain calculations. For the cells in c) and d) the a-b plane spans the (001) and (111) pseudocubic planes respectively. For quadratic strain we have $a = b$, which are the locked in-plane lattice parameters, while c is the free to relax out-of-plane lattice parameter and a_{pc} denotes the pseudocubic lattice parameter.

a) [100]-rotation   [010]-rotation   [001]-rotation

b) [1$\bar{1}$0]-rotation   [11$\bar{2}$]-rotation   [111]-rotation
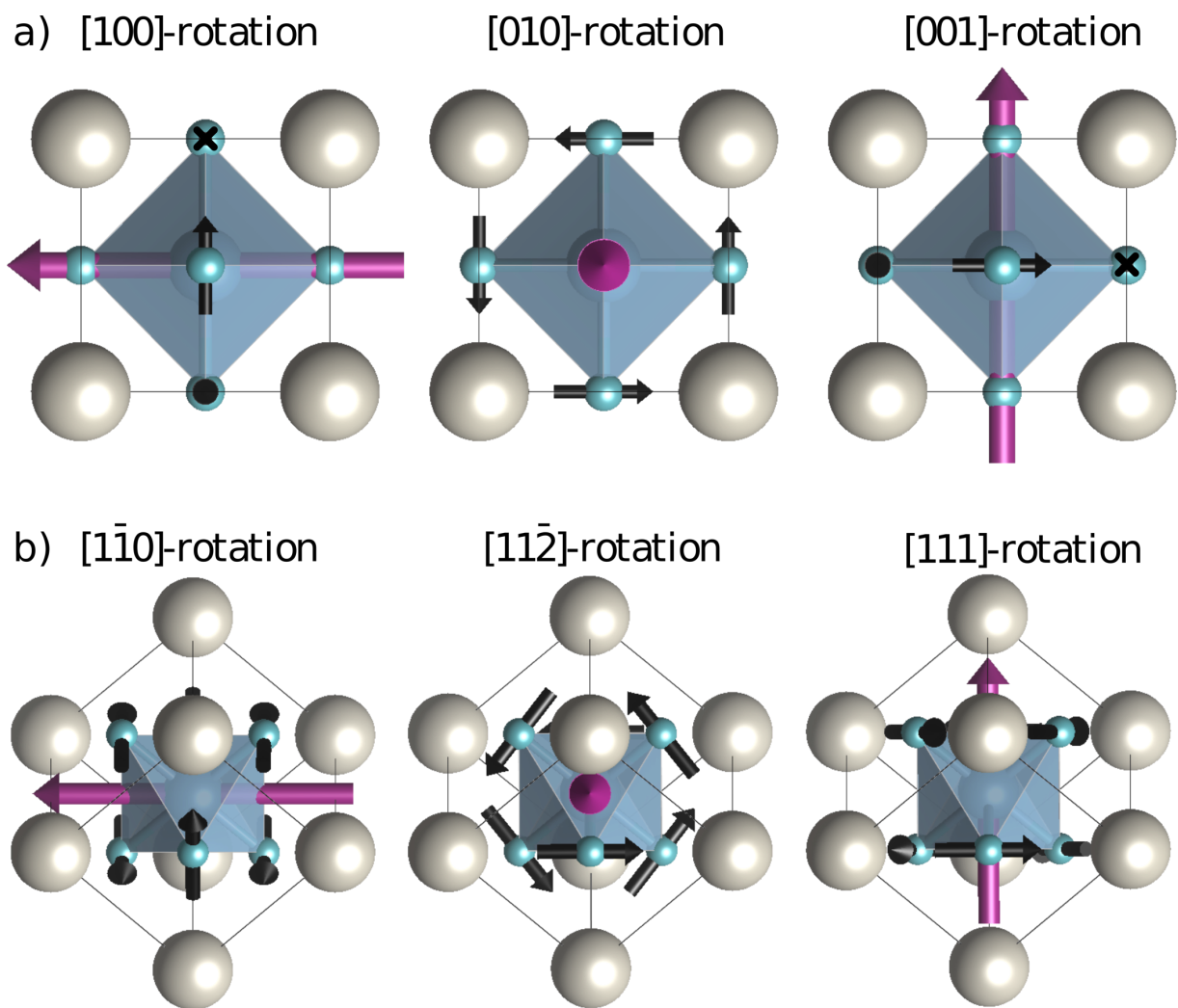
FIG 2, illustration of the in-plane and out-of-plane rotational modes under a) (001)-strain and b) (111)-strain. For (001)-strain, [100] and [010] are in-plane while [001] is out-of-plane. For (111)-strain [1$\bar{1}$0] and [11$\bar{2}$] are in-plane, while [111] is out-of-plane.
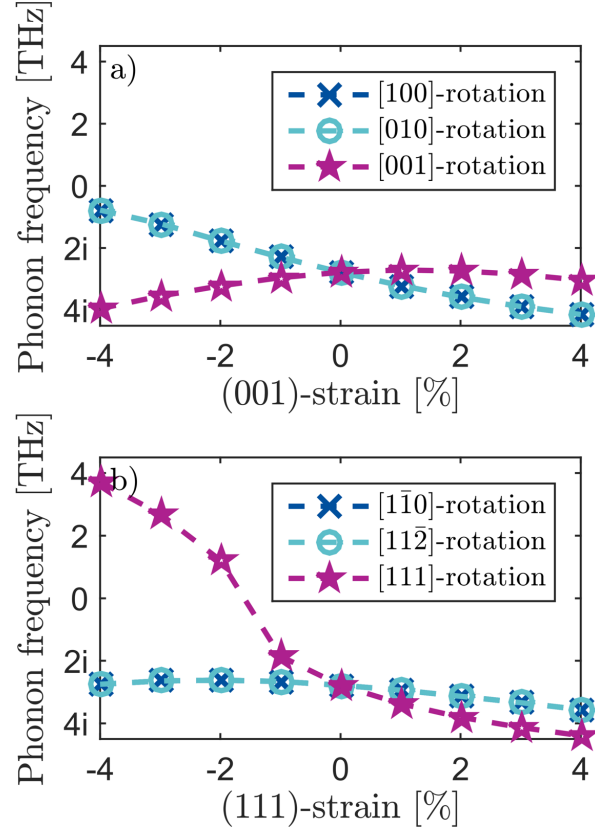
FIG 3, phonon frequencies for the different rotational modes as a function a) (001)-strain and b) (111)-strain. Illustrations of the different rotational modes are shown in Fig. 2. The dashed lines are guides to they eye.
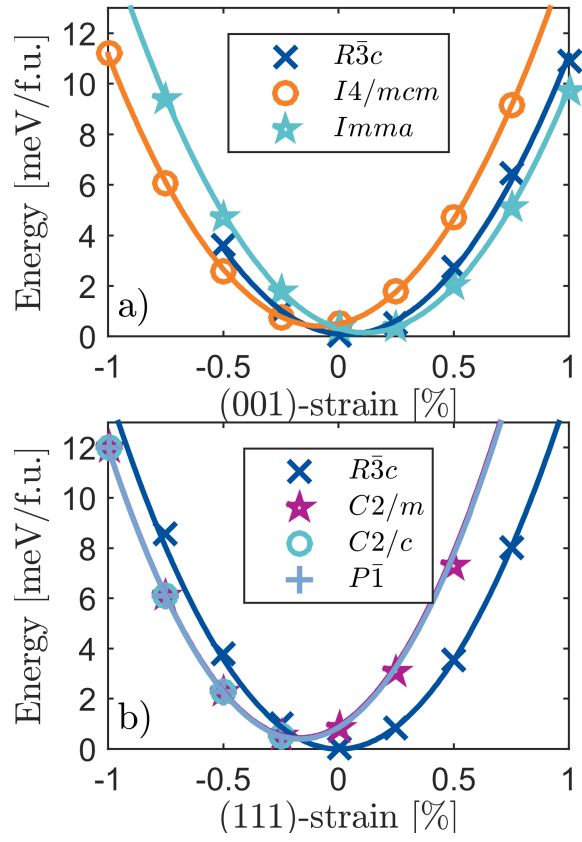
FIG 4, energy vs strain for the different phases. a) (001)-strain, b) (111)-strain. The solid lines correspond to fits to parabolic functions as described in the text. The data points correspond to the strain values where the respective phases were stable under geometry optimization.
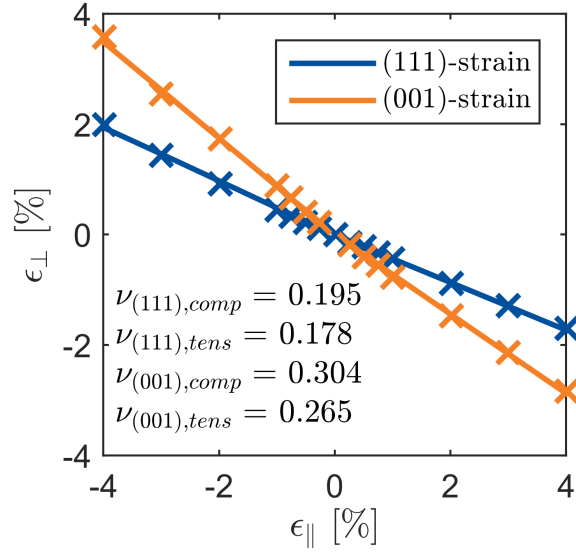
FIG 5, out-of-plane vs in-plane strain for the (001)- and (111)-plane. The different Poisson's ratios ν are calculated from the linear fits to the data. For (001)-strain the 0-percent strain point is from another space group, and hence is not included in any of the fitted lines. For tensile (111)-strain, the different degenerate phases relaxes to the same out-of-plane lattice parameter, thus the they have the same ν.
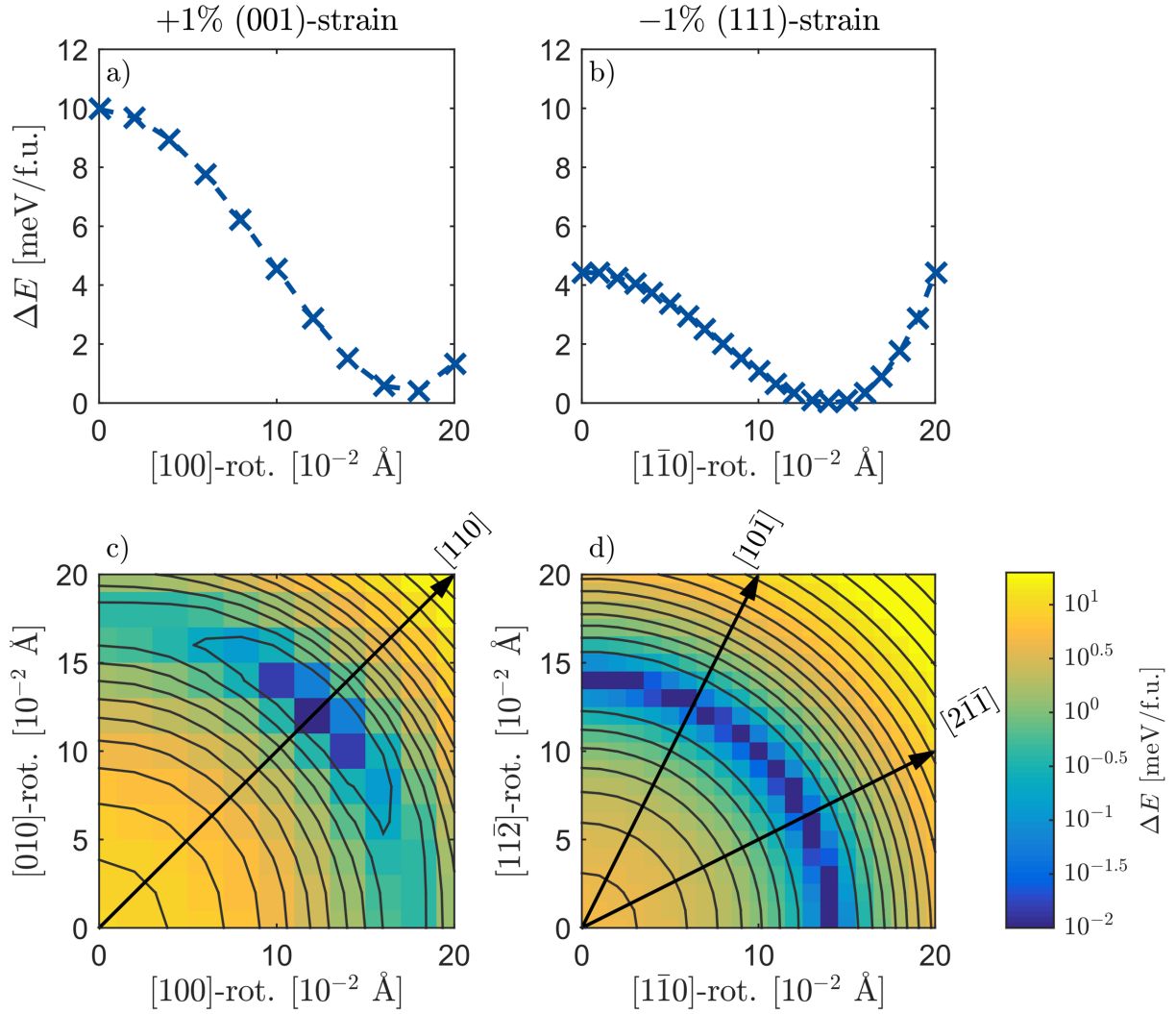
FIG 6, energy difference with respect to the global minimum as a function of mode amplitude for the in-plane rotational modes. a) 1 % tensile (001)-strain where the [100] in-plane rotation mode with $Fmmm$ symmetry is frozen in (the [010] mode is degenerate for all amplitudes). b) 1 % compressive (111)-strain where the [1$\bar{1}$0] phonon mode with symmetry $C2/m$ is frozen in. (the [11$\bar{2}$]-mode with $C2/c$ symmetry is degenerate for all amplitudes). c) Logarithmic energy difference for 1 % tensile (001)-strain when both the degenerate in-plane rotational modes, [100] and [010], are frozen in simultaneously. A global energy minimum is observed for a single point with equal amplitude of [100]- and [010]-rotations, giving $Imma$ symmetry. d) Logarithmic energy difference for 1 % compressive (111)-strain when both the degenerate in-plane rotational modes [1$\bar{1}$0] and [11$\bar{2}$], are frozen in simultaneously. The global energy minimum is no longer a single point but a circle with constant mode amplitude resembling a Mexican hat potential. For c) and d), each pixel represents the energy from one calculation, the black lines are contour plots of the energy landscape while the arrows show the relationship to other high symmetry directions.
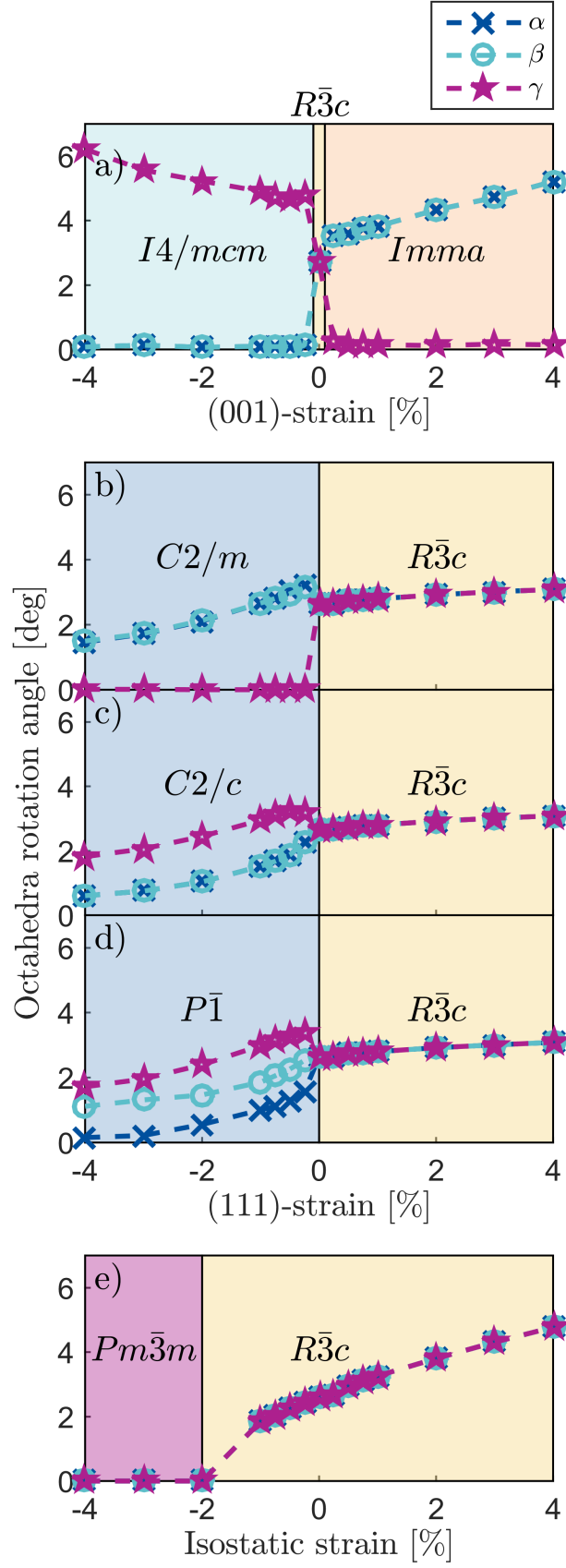
FIG 7, a) pseudocubic octahedral rotation angles vs (001)-strain, b-d) (111)-strain. e) isostatic strain. α, β and γ are defined in Fig. 1. The colors and labels represent which space group has the lowest

energy in this strain range. b-d) shows the response for the three different space groups which are degenerate under compressive strain in the (111)-direction, note that the response is equal for tensile strain. For the $P\bar{1}$ symmetry in d) one arbitrary combination of $[1\bar{1}0]$- and $[11\bar{2}]$-rotation is shown. The dashed lines are guides to the eye.
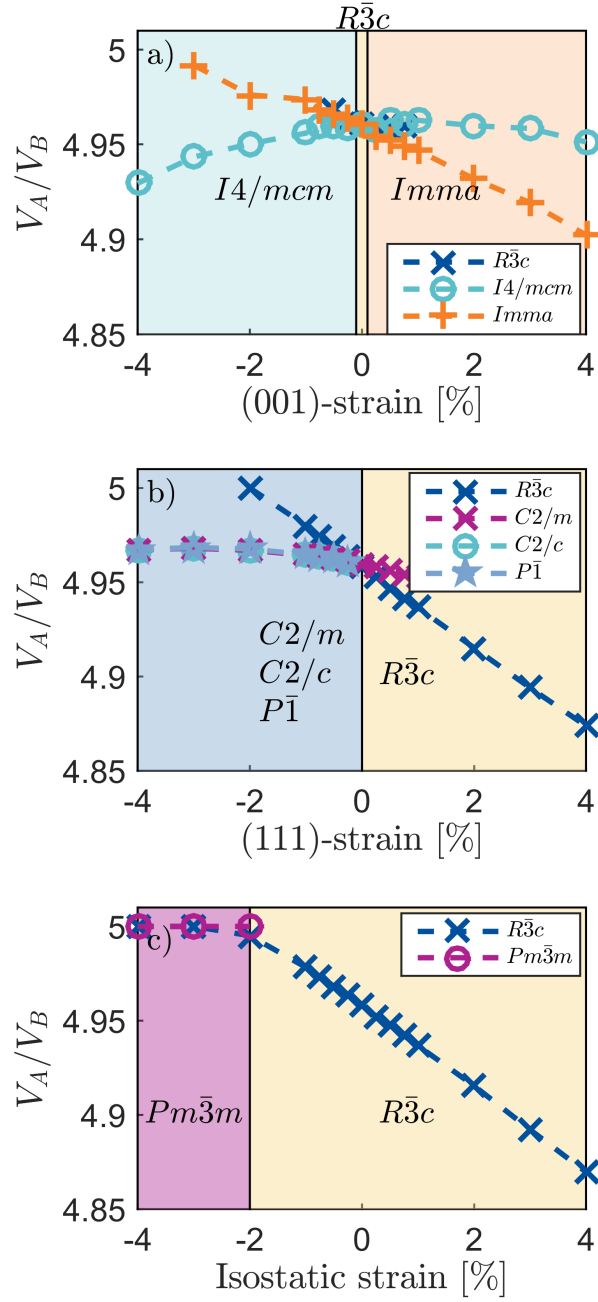
FIG 8, polyhedral volume ratio as function of strain. a) (001)-strain, b) (111)-strain, c) isostatic strain. The colors and labels represents which space groups has the lowest energy in this strain range. $V_A/V_B = 5$ for the un-rotated cubic phase, and then decreases from this value as the distortions are increased. The dashed lines are guides to the eye.
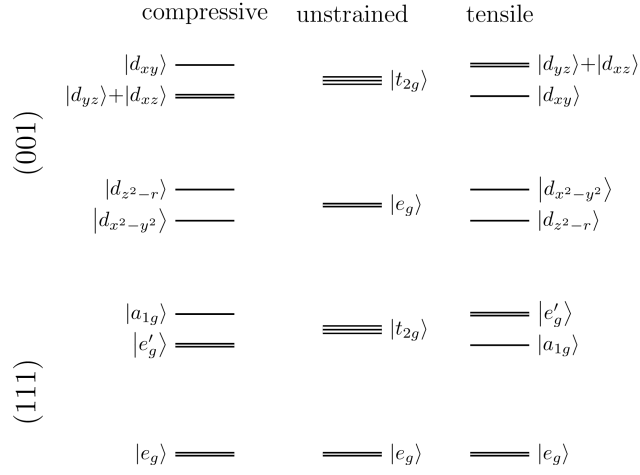
FIG 9, splitting of d-states of dodecahedral coordinated sites for (001)- and (111)-strain. Note that e_g and t_{2g} levels are reversed for dodecahedral sites compared to octahedral sites. The trigonal distortion from (111)-strain splits the t_{2g} levels into a_{1g} and $e_g{}'$ which are superpositions of the d_{xy}, d_{yz} and d_{xz} states.[44]
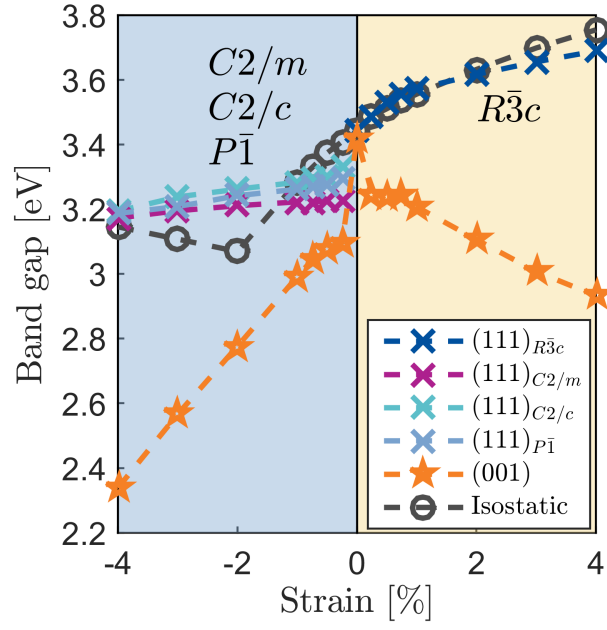
FIG 10, PBE-sol band gap of the different structures as a function of different strain. The colors and labels corresponds to which space groups are stable for (111)-strain in the given strain range. For (001)-strain there is a change in symmetry at 0 % strain, while for isostatic strain there is a change in symmetry at -2 % strain. For the $P\bar{1}$ symmetry we have selected the same arbitrary combination of $[1\bar{1}0]$- and $[11\bar{2}]$-rotation as in Fig. 7 d). The dashed lines are guides to the eye.
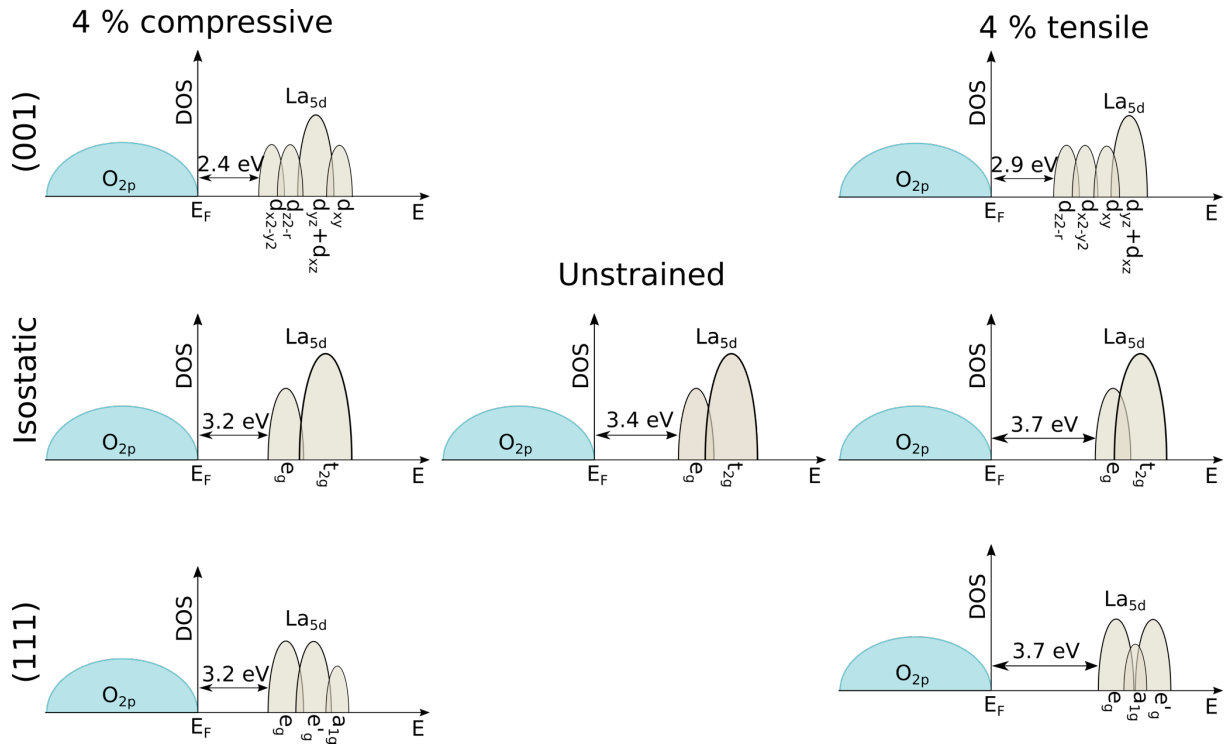
FIG 11, Schematic density of states showing the splitting of the La$_{5d}$ states under (001)-, isostatic- and (111)-strain. It is further shown how the splitting are related to the changes in band gap when LAO is strained.